ACS Catalysis

pubs.acs.org/acscatalysis

Research Article

Cobalt–Nickel Nanoparticles Supported on Reducible Oxides as Fischer–Tropsch Catalysts

Carlos Hernández Mejía, Jessi E. S. van der Hoeven, Petra E. de Jongh, and Krijn P. de Jong*

Cite This: *ACS Catal.* 2020, 10, 7343–7354

Read Online

ACCESS | Metrics & More | Article Recommendations | Supporting Information

ABSTRACT: Efficient and more sustainable production of transportation fuels is key to fulfill the ever-increasing global demand. In order to achieve this, progress in the development of highly active and selective catalysts is fundamental. The combination of bimetallic nanoparticles and reactive support materials offers unique and complex interactions that can be exploited for improved catalyst performance. Here, we report on cobalt–nickel nanoparticles on reducible metal oxides as support material for enhanced performance in the Fischer–Tropsch synthesis. For this, different cobalt to nickel ratios (Ni/(Ni + Co): 0.0, 0.25, 0.50, 0.75, or 1.0 atom/atom) supported on reducible (TiO_2 and Nb_2O_5) or nonreducible (α-Al_2O_3) oxides were studied. At 1 bar, Co–Ni nanoparticles supported on TiO_2 and Nb_2O_5 showed stable catalytic performance, high activities and remarkably high selectivities for long-chain hydrocarbons (C_{5+}, ~80 wt %). In contrast, catalysts supported on α-Al_2O_3 independently of the metal composition showed lower activities, high methane production, and considerable deactivation throughout the experiment. At 20 bar, the combination of cobalt and nickel supported on reducible oxides allowed for 25–50% cobalt substitution by nickel with increased Fischer–Tropsch activity and without sacrificing much C_{5+} selectivity. STEM-EDX and IR of adsorbed CO pointed to a cobalt enrichment of the nanoparticle's surface and a weaker adsorption of CO in Co–Ni supported on TiO_2 and Nb_2O_5 and not on α-Al_2O_3, modifying the rate-determining step and the catalytic performance. Overall, we show the strong effect and potential of reducible metal oxides as support materials for bimetallic nanoparticles for enhanced catalytic performance.

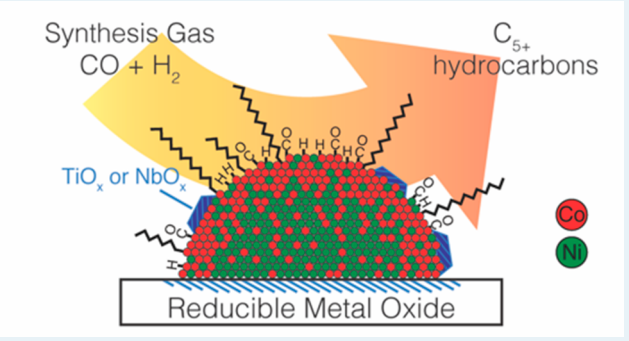

KEYWORDS: *bimetallics, SMSI, Fischer–Tropsch synthesis, support effects, reducible oxides, metal–support interaction*

1. INTRODUCTION

The increasing demand for transportation fuels has stimulated the diversification of their sources and encouraged research towards efficient production.[1,2] Liquid fuels in particular have been widely employed due to their high energy density and convenience to handle.[3] Fuels produced from processes such as gas-to-liquids (GTL) or coal-to-liquids (CTL) have emerged as an attractive alternative to the traditional fuels derived from crude oil. The GTL and CTL processes allow feedstock diversification and generation of ultraclean fuels. A crucial step in GTL and CTL is the catalytic transformation of synthesis gas (a mixture of carbon monoxide and hydrogen) to hydrocarbons, also known as the Fischer–Tropsch (FT) synthesis. The competitiveness of FT, and therefore the GTL and CTL processes, heavily relies on highly productive and stable catalysts. Finding materials with improved FT catalytic performance is highly desirable.

The FT synthesis is a complex reaction that is typically catalyzed by late-transition metals in the metallic or carbidic form. Current research has shown that the rate-controlling step in such catalytic surfaces need a balance between CO dissociation, water removal, chain growth and chain-growth termination for optimal FT perfomrance.[4−6] However, no single metal surface displays these characteristics concurrently.[4] Bimetallic systems hold potential to bring about unique catalytic properties distinct from those of the individual metals.[7−10]

Nowadays, cobalt-based FT catalysts are employed in GTL due to their selectivity toward long-chain hydrocarbons (C_{5+}), low water–gas-shift activity, stable performance, and costs.[11,12] Considering these characteristics, iron, nickel, or copper are potential candidates to form bimetallic catalysts with cobalt. Taking into account the industrial FT conditions, that is, temperatures between 200 and 250 °C and pressures 10–40 bar, CO dissociation on copper is not favored and thus Co–

Received: February 14, 2020
Revised: May 15, 2020
Published: June 9, 2020

https://dx.doi.org/10.1021/acscatal.0c00777
ACS Catal. 2020, 10, 7343–7354

Cu systems can be employed for the synthesis of alcohols.[13−15] Iron under FT conditions often favors the formation of iron carbide that might lead to segregation in Co−Fe systems and loss of possible bimetallic synergy.[16,17] Finally, nickel can readily dissociate CO and form stable Co−Ni alloys, making it an attractive option. However, risks exist of lower C_{5+} selectivity due to high hydrogenation activity and concomitant methane production and decreased stability due to formation of volatile nickel tetracarbonyl.[18] Indeed, in most previous reports a compromise between activity and C_{5+} selectivity has been observed for Co−Ni-based FT catalysts, although a common feature has been the utilization of nonreducible supports, such as silica, alumina, or zirconia.[19−24] Early work of Arai et al.[25−28] has shown that the nature of the support has important consequences for the FT performance of Co−Ni catalysts; they observed differences in catalytic performance from supports with contrasting electronegativities but similar performance of reducible and nonreducible supports.

The interaction between metal nanoparticles and the support has become a prominent tool in the design of catalysts with enhanced performance.[29,30] For bimetallic nanoparticles, the interaction with the support can also lead to various and usually complex phenomena that strongly affect their catalytic performance.[31−35] The understanding of such interactions is often difficult. One of the phenomena that arises from the interaction of mono- and bimetallic nanoparticles supported on reducible metal oxides (e.g., TiO_2, Nb_2O_5, CeO_2, etc.) is the so-called strong metal−support interaction (SMSI).[36,37] This phenomenon takes place upon partial reduction of the support at the periphery of the metal nanoparticle, leading to the generation of mobile suboxide species (e.g., TiO_x, NbO_x) that partially cover the surface of the metal nanoparticle. In FT, reducible oxidic supports have a major influence on the catalyst performance.[38,39] The mild Lewis acidity of the suboxides is known to promote intrinsic surface-specific catalytic activity (turnover frequency, TOF) and selectivity toward C_{5+} products.[40] The increased TOF is believed to originate at the interphase between the suboxides and the metal where an enhanced CO adsorption and rate of hydrogenation occurs.[41,42] Tuning this interaction can lead, for instance, to cobalt-based catalysts with enhanced FT activities,[43] and in the case of nickel-based catalysts, SMSI can be employed to suppress the formation of nickel tetracarbonyl and enhance the selectivity toward longer hydrocarbons.[44,45] Hence, improvement can be achieved by careful selection of the components in the Co−Ni catalytic system, particularly of the support material.

In this research, we investigated the effect of cobalt substitution by nickel on supported FT catalysts and the influence of the support nature on the catalytic behavior of the metals. Several characterization techniques, in particular IR spectroscopy of adsorbed CO, were employed to elucidate the effect of combining cobalt and nickel on the different supports. At 1 bar, the Co−Ni samples displayed increased activities and C_{5+} selectivities, up to doubling the activity compared to the monometallic catalysts. Contrastingly, α-Al_2O_3-supported catalysts had for all Co−Ni compositions lower metal-normalized activities and higher selectivities toward methane. Moreover, these catalysts deactivated severely throughout the experiment in contrast to the more stable TiO_2- and Nb_2O_5-supported catalysts. Increasing synthesis gas pressure to 20 bar benefited the activity and selectivity of the samples supported on reducible oxides with high cobalt content, and with similar C_{5+} selectivities as the monometallic cobalt-based catalysts. Reducible oxides used as support material strongly modified the reactivity of alloys, opening new possibilities for more efficient catalysts in general.

2. EXPERIMENTAL METHODS

2.1. Catalyst Preparation. Niobia (Nb_2O_5) and titania (TiO_2) were employed as reducible supports. Nb_2O_5 was obtained by crystallization of niobium oxide hydrate (Nb_2O_5·nH_2O, HY-340, AD/4465 provided by Companhia Brasileira de Metalurgia e Mineração, CBMM). Crystallization was carried out in stagnant air at 600 °C (5 °C·min^{-1}, 4 h). The obtained Nb_2O_5 had a pseudohexagonal TT-phase, a specific surface area of 9 m^2·g^{-1}, and a specific mesopore volume of 0.05 cm^3·g^{-1}. TiO_2 had a rutile phase, a specific surface area of 11 m^2·g^{-1}, and a specific mesopore volume of 0.04 cm^3·g^{-1}. α-Alumina (α-Al_2O_3) was employed as nonreducible support and supplied by BASF in the form of extrudates. The α-Al_2O_3 consisted of only α-phase with specific surface area of 7 m^2·g^{-1} and specific mesopore volume of 0.02 cm^3·g^{-1}. Support materials were crushed and sieved (75−150 μm grains) prior to catalyst preparation.

The supported metal catalysts were prepared using the incipient wetness impregnation method. First, 2.0 g of support material was dried under vacuum at 80 °C for 1 h; thereafter the impregnation was performed at room temperature with a 4.2 M aqueous solution with the appropriate cobalt−nickel ratio. The aqueous solutions were prepared using $Ni(NO_3)_2$·$6H_2O$ (Acros, 99+%) and $Co(NO_3)_2$·$6H_2O$ (Acros, 99+%) in Milli-Q water. After impregnation, the materials were dried at 60 °C (5 °C·min^{-1}, 2 h) in a fixed bed reactor under N_2 flow and subsequently calcined at 350 °C (3 °C·min^{-1}, 2 h). Metal loadings were defined as the total mass of metallic Ni or Co or both per gram of reduced catalyst, resulting in total metal loadings of 6−8 wt % (Table S1). The total metal loading per support was chosen in order to maintain similar metal loadings per unit surface area within all the samples. In this way, the metal distribution over the different supports is expected to be similar. The metal composition is expressed as Ni/(Ni + Co) atomic ratio and the ratios studied were 0.0, 0.25, 0.5, 0.75, and 1.0 atom/atom.

2.2. Characterization. Temperature-programmed reduction (TPR) analyses were performed using a Micromeritics Autochem 2990 instrument, where typically 50 mg of sample (75−150 μm grains) were dried at 120 °C for 1 h in Ar flow followed by reduction from room temperature up to 600 °C (5 °C·min^{-1}) in a 5 vol % H_2/Ar flow.

Bright field transmission electron microscopy (TEM) and dark field scanning transmission electron microscopy (STEM-EDX) images were acquired at a FEI Talos F200X microscope operated at 200 kV equipped with 4 energy dispersive X-ray (EDX) detectors, a high-angle annular dark-field (HAADF) and a bright field detector. The reduced and subsequently passivated samples for the microscopy analysis were prepared by suspending the catalysts in 2-propanol (>99.9%, Sigma-Aldrich) using sonication and drop casting the suspension on a Cu TEM grid (200 mesh copper (100), Formvar/carbon film). The metal particle size measurements and Co−Ni distribution cross-section analyses were carried out using the ImageJ[46] software by analyzing at least 500 particles. Particle surface average diameters or Sauter mean ($D[3,2]$) were then calculated and corrected for a 2 nm oxide shell. The theoretical H_2-uptake ($\mu mol_{H_2}·g_{metal}^{-1}$) was calculated by first obtaining

https://dx.doi.org/10.1021/acscatal.0c00777
ACS Catal. 2020, 10, 7343−7354

the specific metallic surface area ($m^2 \cdot g^{-1}_{metal}$) from $D[3,2]$ (nm) from TEM and assuming hemispherical particles:

$$\text{specifc metallic surface area} = \frac{6}{(10^6\rho)(10^{-9}D[3,2])}$$

where ρ is the density (8.9 $g \cdot cm^{-3}$) for cobalt and nickel. Then, assuming an average metal cross-sectional area of 0.0656 nm^2, a metal to H stoichiometry of 1, and N_A = 6.0221 × 10^{23} mol^{-1}:

$$\text{theoretical } H_2 \text{ uptake} = \frac{\text{specific metallic surface area}}{2N_A(10^{-18} \times \text{metal cross-section area})}$$

H_2 chemisorption was measured on a Micromeritics ASAP 2020C using ∼100 mg of sample. Prior to the measurement, the sample was reduced in pure H_2 at 350 °C (5 °C·min^{-1}, 2 h). The sample was then evacuated and cooled to 150 °C, and H_2 chemisorption was measured at that temperature. Inductively coupled plasma-optical emission spectroscopy (ICP-OES) was performed on a SPECTRO ARCOS in order to establish the cobalt to nickel ratio before and after catalysis; samples were extracted using aqua regia.

Fourier transform infrared (FT-IR) spectroscopy measurements were carried out in a PerkinElmer 2000 instrument, in a specially designed cell fitted with CaF_2 windows. Self-supported catalyst wafers were prepared by applying on a powdered sample a force of 4000 kg for 20 s, yielding a wafer of 1 cm diameter, and <1 mm thickness. Before dosing CO, the wafer sample was placed in the FTIR cell and reduced using a flow of pure hydrogen at 350 °C (5 °C·min^{-1}, 2 h); then at the same temperature the hydrogen flow was stopped and evacuated to ∼10^{-5} mbar. Thereafter the sample was cooled down to 220 °C under dynamic vacuum and left for 1 h. A 10 vol % CO in He mixture was slowly introduced into the cell until the pressure reached ∼10^{-4} mbar and allowed to equilibrate for 5 min to collect the spectrum. The CO/He mixture was slowly further introduced to reach various pressures up to 1 bar, and spectra were measured at these different pressures after equilibration for 5 min before each measurement. For treatment of the data, the measured spectra were normalized by the total available metal sites per sample as obtained from H_2 chemisorption. Areas resulting from the deconvolution in the bimetallic samples were normalized to the area of the corresponding monometallic sample.

2.3. Catalytic Performance. The low-pressure catalytic performance was assessed in a quartz glass plug-flow reactor, loaded with ∼20 mg of catalyst (38−150 μm) diluted with ∼200 mg of SiC (212−425 μm). Catalysts were reduced in situ at 350 °C (5 °C·min^{-1}, 2 h) in an Ar/H_2 = 2 v/v flow (GHSV = 60000 h^{-1}) at 1 bar. After reduction, the sample was cooled down to 220 °C, and once the temperature was reached, the gas composition was changed to synthesis gas (H_2/CO = 2 v/v, GHSV = 20000 h^{-1}) maintaining 1 bar total pressure. CO conversion was below 5%, and the reaction was carried out for 40 h. C_1−C_{18} products were analyzed by online gas chromatography (Varian 430 GC, CP sil-5 column). After reaction, the synthesis gas flow was changed for argon, and the reactor was cooled down to room temperature.

The high-pressure catalytic performance was measured using an Avantium Flowrence 16 parallel reactor setup. Stainless steel reactors (ID = 2 mm) were loaded with 50−100 mg of catalyst (38−150 μm) and diluted with 200 mg of SiC (212−425 μm). Prior to reaction, the catalysts were reduced *in situ* at 350 °C (1 °C·min^{-1}, 8 h) in 25 vol % H_2 in He at 1 bar. After reduction, the temperature was lowered to 220, 240, or 260 °C (3 °C·min^{-1}), and the pressure was increased to 20 bar under H_2 flow. Synthesis gas (H_2/CO = 2 v/v, 5 vol % He as internal standard) was then introduced. The product stream was analyzed online with an Agilent 7890A GC, hydrocarbon products were analyzed on an Agilent J&W PoraBOND Q column connected to an FID, and the permanent gases were separated on a ShinCarbon ST column and quantified using a TCD.

3. RESULTS AND DISCUSSION

3.1. Catalyst Characterization. After calcination, samples were characterized by temperature-programmed reduction (TPR) under hydrogen flow, and the corresponding reduction profiles are shown in Figure 1. Samples containing only cobalt

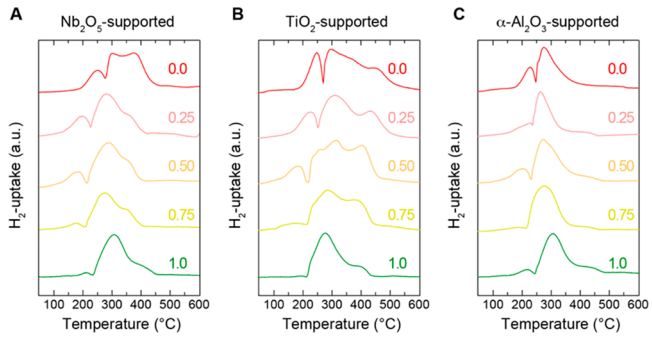

Figure 1. Temperature-programmed reduction (TPR) profiles of the Co−Ni oxide samples supported on niobia (A), titania (B), or α-alumina (C). The metal composition Ni/(Ni + Co) atom/atom is indicated for each profile.

(Ni/(Ni + Co) = 0.0 atom/atom) show two distinctive H_2-uptake peaks; the first one corresponds to the reduction of Co_3O_4 to CoO and the second one to the reduction of CoO to metallic cobalt. For the reducible supports (Figure1A,B), the first reduction event appears at ∼250 °C, and the second one shows two overlapping peaks that finalize at temperatures around 400−500 °C. The alumina-supported sample shows a first reduction event at 225 °C, and reduction is complete at 350 °C (Figure 1C). Partial replacement of cobalt with nickel (Ni/(Ni + Co) = 0.25, 0.5, and 0.75 atom/atom) shifted the reduction profiles to lower temperatures, which indicates an influence of the presence of nickel on the cobalt oxide reduction. This influence was more pronounced on the reducible supports than on the nonreducible support. The lowest reduction temperature for the supported cobalt−nickel oxides was observed for the Ni/(Ni + Co) = 0.75 atom/atom sample in the case of the reducible supports and 0.5 atom/atom for the nonreducible support. Moreover, the intensity of the first reduction step decreased gradually when increasing the cobalt substitution, likely due to the decreased amount of Co^{3+} species. Total substitution of cobalt by nickel (Ni/(Ni + Co) = 1.0 atom/atom) showed a slight increase of the temperatures in the reduction profile of nickel oxide to metallic nickel compared to the bimetallic samples.

Quantification from the reduction profiles revealed a decrease in the molar ratio of H_2 consumption to metal loading upon replacement of cobalt with nickel (Table S1). For the three supports, monometallic cobalt samples had an

https://dx.doi.org/10.1021/acscatal.0c00777
ACS Catal. 2020, 10, 7343−7354

H_2/Co molar ratio of 1.4, closely corresponding to a 1.3 ratio expected for the full reduction of Co_3O_4 to metallic Co, and monometallic nickel samples had an H_2/Ni molar ratio of 1.0, which corresponds to the reduction of NiO to Ni. The bimetallic samples showed intermediate values, indicative of a mix of Co^{3+}, Co^{2+}, and Ni^{2+} species. Overall, the mixed cobalt and nickel oxides formed after coimpregnation and subsequent calcination displayed lower reduction temperatures than the monometallic samples, particularly in the case of the samples supported on reducible oxides.

Based on the TPR results, samples were treated under hydrogen flow at 350 °C to reduce the cobalt and nickel oxides to the metallic form, and thereafter H_2 chemisorption measurements were carried out. Hydrogen uptake results indicate that gradual replacement of cobalt with nickel increased the adsorption of hydrogen (Table 1), suggesting an increased metal dispersion over the support. The effect seemed more pronounced for the α-alumina-supported samples. After the experiments, samples were exposed to air at room temperature and analyzed by scanning transmission electron microscopy (STEM), and their metal particles sizes (D[3,2]) were determined (Table 1). STEM analyses revealed a gradual decrease in particle size when cobalt was substituted by nickel for all three supports. Figure 2 shows a more uniform distribution of the metal nanoparticles over Nb_2O_5 facilitated seemingly by the presence of nickel. The smallest particles were obtained at intermediate Co−Ni compositions, that is, at Ni/(Ni + Co) of 0.5 atom/atom for TiO_2 and 0.75 atom/atom for Nb_2O_5 and α-Al_2O_3. Thus, metal nanoparticle dispersion on the oxidic supports was enhanced by addition of nickel, as suggested by the H_2 chemisorption measurements and in accordance with previous reports.[20,47]

Table 1. Summary of the Experimental H_2-Uptake Determined by H_2-Chemisorption Measurements and STEM-Derived Particle Diameter (D[3,2]) of the Samples after the Chemisorption Experiments with the Corresponding Theoretical H_2-Uptake based on the Particle Diameter from STEM

		H_2-chemisorption	STEM	
support	Ni/(Ni + Co) (atom/atom)	experimental H_2-uptake ($\mu mol_{H_2} \cdot g_{metal}^{-1}$)	D[3,2] (nm)	theoretical H_2-uptake ($\mu mol_{H_2} \cdot g_{metal}^{-1}$)
Nb_2O_5	0.0	320	17	491
	0.25	441	13	658
	0.50	452	10	813
	0.75	482	9	912
	1.0	362	10	873
TiO_2	0.0	464	15	569
	0.25	573	12	700
	0.50	647	9	908
	0.75	622	10	899
	1.0	621	10	857
α-Al_2O_3	0.0	610	13	657
	0.25	731	11	799
	0.50	888	9	967
	0.75	1101	8	1115
	1.0	1056	9	949

Theoretical hydrogen uptake was calculated using the corresponding STEM-derived particle sizes (Table 1). A comparison between theoretical H_2-uptake and experimental H_2-uptake, obtained from H_2 chemisorption measurements, shows significant discrepancies for the niobia- and titania-supported samples (Table 1, Figure S1A,B). The differences are larger for the niobia-supported samples than for the titania-supported ones and increase with increasing nickel content in the samples. Since Nb_2O_5 and TiO_2 are both reducible oxides, the discrepancies are ascribed to the strong metal−support interaction (SMSI) effect, which means that suboxides from the support generated upon reduction treatment partially cover the metallic nanoparticles, thus decreasing the available metallic surface area.[36,48] The niobia-supported nanoparticles were more strongly affected by this than the titania-supported ones. Moreover, the increasing discrepancies with increasing Ni content may point to stronger susceptibility to SMSI for Ni than for Co or relate to the decrease in particle size.[49] In contrast, the samples supported on α-Al_2O_3, which is a nonreducible support and hence does not display the SMSI effect, showed similar values for theoretical and experimental hydrogen uptake (Table 1, Figure S1C).

Characterization of metal nanoparticles supported on transition metal oxides by transmission electron microscopy in dark-field or bright-field is difficult due to the similar transition metal atomic number and material density, respectively, of each component (Figure 2A,C,E). Moreover, supported bimetallic nanoparticles pose a challenge to discern the distribution of the individual elements. EDX mapping combined with STEM has therefore become a powerful tool to better study these materials.[50] STEM-EDX of the bimetallic samples after reduction at 350 °C and passivation at room temperature showed that, independently of the metal composition, nickel associated with cobalt (Figures 2D and S2A−C); however cobalt was sometimes found without nickel, being more pronounced for the samples with more cobalt (Ni/(Ni + Co) = 0.25 atom/atom). This is better visible at higher magnification as shown in Figure S3A. For the nanoparticles containing both metals, a cross-section analysis of several particles (Figures S4 and S5) confirmed a homogeneous distribution of cobalt and nickel, implying the formation of a uniform alloy after reduction at 350 °C and passivation. Similar observations were made for the titania- and alumina-supported samples (Figures S6A and S7A).

Further characterization by FT-IR spectroscopy with CO as a probe molecule was carried out in order to examine the electronic and structural surface properties of the metals and alloys. After reduction at 350 °C under hydrogen flow of the self-supported catalyst wafer and cooling down to 220 °C under ultrahigh vacuum, CO was dosed from 1×10^{-4} to 100 mbar. Figure S8 shows the spectra in the frequency region between 2250 and 1550 cm^{-1} for various Co−Ni compositions supported on niobia, titania and α-alumina at increasing CO pressures. Examples of the spectra of the niobia-, titania-, and α-alumina-supported samples at 1×10^{-1} mbar CO pressure are as well shown in Figure 3. For the monometallic cobalt samples (Ni/(Ni + Co) = 0.0 atom/atom), a single narrow band is observed at low pressures around 1980 cm^{-1}, increasing in intensity upon higher CO pressure, due to higher CO coverages. A second broad band around 1800 cm^{-1} appears at $P_{CO} = 1 \times 10^{-2}$ mbar. According to the literature, the narrow band at high wavenumbers can be ascribed to linearly adsorbed CO and the broad band at lower wavenumbers to CO adsorbed in bridged mode.[51−54] At intermediate pressures (P_{CO} = 1 mbar), a new band next to the linearly adsorbed CO band appeared around 2060 cm^{-1},

https://dx.doi.org/10.1021/acscatal.0c00777
ACS Catal. 2020, 10, 7343−7354

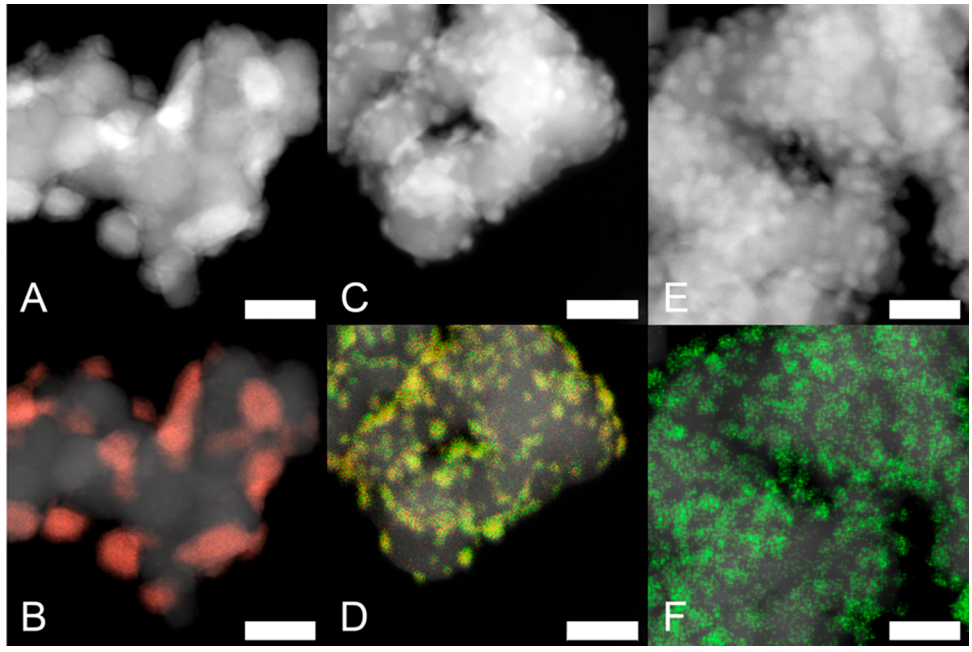

Figure 2. STEM-EDX of monometallic cobalt (A, B), bimetallic cobalt−nickel (C, D, nominal Ni/(Ni + Co) = 0.50 atom/atom), and monometallic nickel (E, F) samples supported on niobia after reduction at 350 °C and passivation at room temperature. Panels A, C, and E show the dark-field STEM images, and panels B, D, and F show the same dark-field images overlapped with the corresponding EDX maps for cobalt (shown in red) and nickel (shown in green); the scale bars represent 40 nm.

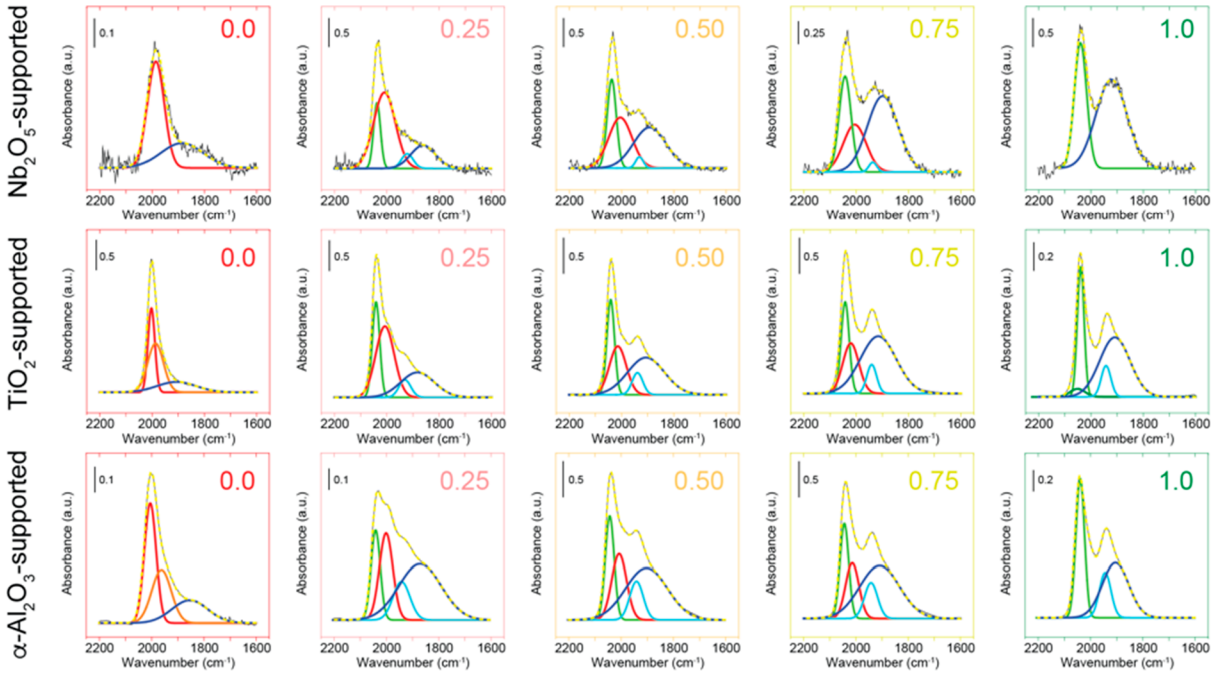

Figure 3. Deconvoluted CO-FTIR spectra of the niobia-, titania-, and α-alumina-supported samples at 0.1 mbar CO pressure and at 220 °C. The corresponding Ni/(Ni + Co) composition is indicated for each spectrum. Spectra are plotted with a black line and curves from the deconvolution correspond to CO linearly adsorbed on cobalt (red and orange), CO linearly adsorbed on nickel (green), CO adsorbed on bridged mode (light and dark blue), and the resulting curve (dashed yellow).

being more clear for the cobalt supported on titania sample. This new band might correspond to CO adsorbed on cobalt in close contact with the support, with a more electropositive character ($Co^{\delta+}$) due to the presence of oxygen at the interface, as previously reported.[51,55,56]

For the monometallic nickel samples (Ni/(Ni + Co) = 1.0 atom/atom) on the other hand, a narrow band (~2020 cm^{-1}) and a broad band (~1850 cm^{-1}) are already observed at the lowest CO pressure. Again, the high wavenumber band can be ascribed to CO adsorbed in linear mode and the lower wavenumber band to bridged CO on nickel.[57−59] Ni appears to favor a CO coordination in bridged mode at low CO surface coverages in line with the appearance of the low-frequency band for nickel at low pressures, in contrast to the cobalt

https://dx.doi.org/10.1021/acscatal.0c00777
ACS Catal. 2020, 10, 7343−7354

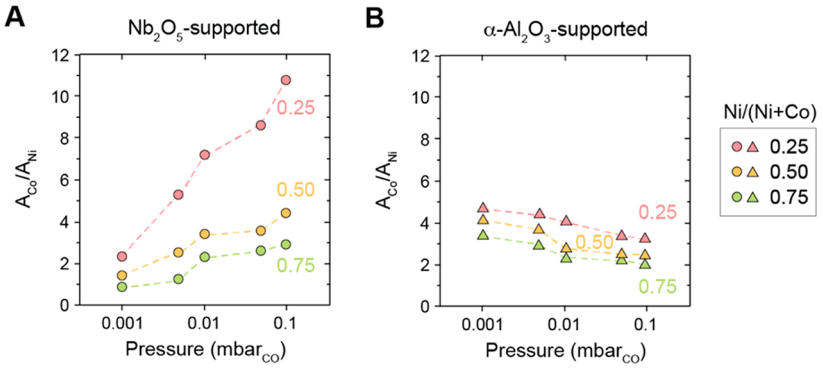

Figure 4. Ratio of the IR band areas of linearly adsorbed CO on cobalt and nickel as a function of CO pressure for bimetallic nanoparticles supported on niobia (A) and α-alumina (B). Measurements were carried out at 220 °C.

samples. The low work function of nickel and higher valence-electron band occupation result in an interaction with CO dominated by $2\pi^*$ back-donation that favors a bridged coordination.[60] An increased intensity and shift to higher wavenumbers is observed for both bands upon increasing the CO pressure, for the linear-CO band to ~2070 cm^{-1} and for the bridge-CO band to ~1920 cm^{-1} together with the appearance of a shoulder at slightly higher wavenumbers. Bands corresponding to subcarbonyl species $Ni(CO)_x$ (x = 2, 3), precursors of volatile nickel tetracarbonyl at 2075−2090 cm^{-1} according to literature,[59,61,62] were not observed at the highest pressure in this set of experiments (P_{CO} = 100 mbar). Thus, loss of nickel during the CO-FTIR measurements is not expected. In the case of the Co−Ni samples, various bands emerge upon CO adsorption consisting of a combination of bands from the ones observed for the monometallic samples. Likewise, the bands increased in intensity and shifted to higher frequencies upon increasing the CO pressure.

Deconvolution of the spectra for all Co−Ni compositions supported on niobia, titania, and α-alumina at 0.1 mbar CO pressure can be found in Figure 3. In order to distinguish between the cobalt and the nickel contributions in the spectra of the bimetallic samples, the analysis focused on the linear-CO bands, since the bands corresponding to CO adsorbed in bridge mode were too broad and difficult to assign. The low-pressure spectra were used because at 1 mbar and higher CO pressures the cobalt and nickel contributions overlapped (Figure S8). Moreover, the low CO pressures and relative high temperature of the samples (220 °C) prevent dipole−dipole coupling between adsorbed CO molecules, which can influence the CO vibration frequency.[63] The spectra and corresponding deconvolution at CO pressures lower than 1 mbar can be found in Figures S9 and S10 for niobia- and α-alumina-supported samples. For the bimetallic samples, it is possible to distinguish the linear-CO contributions from cobalt (red) and nickel (green). Therefore, the ratio of these areas was used to qualitatively correlate to the surface composition upon interaction with CO. Figure 4 shows the change in ratio of the area for cobalt to the area for nickel as a function of CO pressure for samples supported on niobia or alumina. At a CO pressure of 0.001 mbar, the ratio was already different for both support materials, the surface composition for the α-Al_2O_3-supported samples seems to be rather independent of the overall composition, whereas for the Nb_2O_5-supported samples their surface composition was more affected by the overall composition. Furthermore, upon increasing the CO pressure the change in area ratio behaved remarkably differently for each support, for the Nb_2O_5-supported samples it increased, meaning a more Co-rich surface, while for the α-Al_2O_3-supported ones, it decreased meaning a tendency toward a Ni-rich surface. Reported heats of adsorption for CO on Co and on Ni show similar values;[64−69] therefore, a preferred Co or Ni surface segregation upon contact with CO is not expected, indicating in our case that the metal−support interaction is affecting the surface composition of the nanoparticles.

Also changes in frequency were observed for the linear-CO bands as a consequence of Co−Ni composition on the three different supports. Figure S11 shows the wavenumber at maximum absorbance as a function of metal composition for the linear-CO band on cobalt and on nickel at 0.1 mbar. For the band corresponding to CO adsorbed on cobalt, substitution of cobalt by nickel led to a marked increase in the wavenumber. This increase in the C−O stretching frequency corresponds to a stronger C−O bond, due to less back-donation from cobalt in the CO 2π-antibonding orbitals. The change in wavenumber for the band corresponding to CO adsorbed on Ni was less pronounced. The observed wavenumber shifts can then point to a change in the electron density of Ni and in particular Co in the bimetallic samples, indicative of a close Co−Ni contact likely due to formation of alloyed nanoparticles.[57,70,71]

3.2. Catalytic Performance. Catalyst performance was studied at 1 bar total pressure (H_2/CO = 2 v/v) and 220 °C after in situ reduction at 350 °C for 2 h. Figure 5 shows a summary of the catalytic performance after 40 h on stream, and comprehensive data can be found in Table S2. The metal-normalized catalytic activity of the titania- and niobia-supported catalysts proved markedly higher than the activity of the α-alumina-supported samples for all metal compositions (Figure 5A). Furthermore, a large increase in activity is observed for the Co−Ni catalysts supported on reducible oxides with increasing nickel content, reaching the highest activity at Ni/(Ni+Co) = 0.75 atom/atom. On the other hand, samples supported on α-alumina showed little change upon cobalt substitution by nickel, with a slightly lower activity for the nickel-rich samples (Ni/(Ni + Co) = 0.75 and 1.0 atom/atom). Turnover frequencies (TOFs) followed a similar trend (Table S2), in which cobalt substitution by nickel for titania- and niobia-supported catalysts led to higher TOFs, whereas α-alumina-supported catalysts displayed lower TOFs upon addition of nickel. The selectivities of the catalysts were strongly influenced by the nature of the support and the composition of supported metals (Figure 5B−D). Long-chain hydrocarbons (C_{5+}) selectivities surprisingly reached values of

https://dx.doi.org/10.1021/acscatal.0c00777
ACS Catal. 2020, 10, 7343−7354

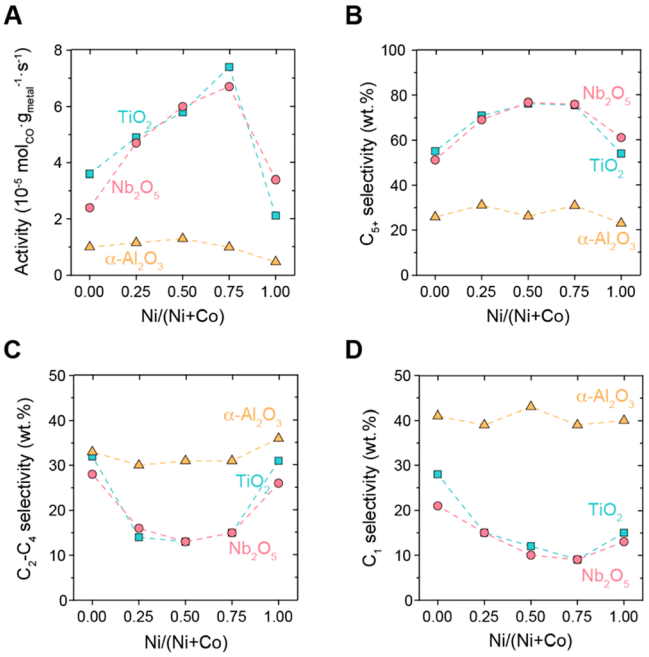

Figure 5. Summary of the catalytic performance after 40 h on stream at 1 bar (H_2/CO = 2 v/v) and 220 °C for samples with various cobalt to nickel ratios supported on reducible (Nb_2O_5 and TiO_2) and nonreducible (α-Al_2O_3) oxides. (A) Activity normalized by total metal weight loading of bi- and monometallic catalysts supported on reducible and nonreducible oxides. The corresponding selectivities for C_{5+}, C_2−C_4, and C_1 products are shown in panels B, C, and D, respectively.

around 80 wt % for the intermediate Co−Ni samples supported on reducible supports, despite the low pressure applied (Figure 5B). In turn, C_1 and C_2−C_4 selectivities were lower in these samples than for the monometallic ones (Figure 5C,D). In stark contrast, α-alumina-supported samples showed low C_{5+} and high C_1 and C_2−C_4 selectivities for all metal compositions. Independently of the nanoparticles' composition, selectivities did not change. Therefore, the exceptionally high C_{5+} selectivities and activities of the catalysts supported on reducible oxides emerged from a combination of nanoparticle composition and nature of the support.

In contrast to our observations, similar FT performance on reducible and nonreducible supports previously reported in the literature[27] might originate from the pretreatment employed, consisting there of a prereduction at 400 °C, likely followed by exposure to air and reduction prior catalysis at 250 °C. These conditions might generate, besides Co−Ni segregation,[72] less suboxides from the reducible supports since the SMSI effect is sensitive to reduction temperature and oxidative conditions.[36,43,73] In turn, a decrease of the promotional catalytic effect might have resulted in a similar performance to the nonreducible-supported catalysts.

The enhanced catalytic performance of the bimetallic catalysts supported on reducible oxides can be better understood when considering the observations by CO-FTIR. First, the interaction with CO led to nanoparticles with a surface enriched in cobalt when supported on reducible oxides and not on the nonreducible oxide (Figure 4). High initial FT activities have been previously observed when bimetallic nanoparticles have been prepared by sequential impregnation forcing a cobalt-enriched surface, in contrast to the samples with a nickel-enriched surface or the monometallic ones.[20]

Second, we have identified a relationship between the wavenumber of maximum absorbance of linear-CO on cobalt and the corresponding TOF based on the experimental H_2 uptake (Figure 6 and Table S3). The set of samples supported

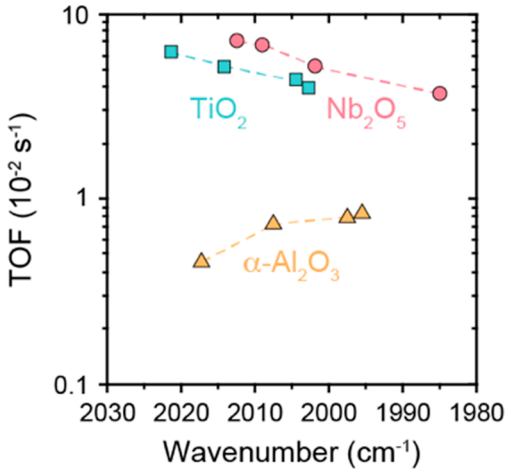

Figure 6. Relationship between turnover frequency (TOF) and wavenumber of linear-CO on cobalt (P_{CO} = 0.1 mbar) for the Co- and CoNi-based catalysts supported on titania, niobia, and α-alumina. TOFs were obtained based on the experimental H_2-uptake derived from H_2-chemisorption and catalytic activity at 40 h on stream (1 bar, H_2/CO = 2 v/v and 220 °C, Table S3).

on α-alumina showed high TOFs as well as low wavenumber values, indicating a stronger CO adsorption to the metal surface and a weaker C−O bond. Thus, higher TOFs here are tentatively ascribed to faster CO dissociation, proposed to be the rate-determining step for the α-alumina-supported samples. This is in agreement with the work of Filot et al.,[4] where in their model Co/α-Al_2O_3 would fall between a regime controlled by the rate of CO dissociation and oxygen removal and addition of nickel (a less oxophilic metal) might move the rate-controlling step away from the oxygen removal regime to the one controlled by CO dissociation. That results in a carbon coverage and concomitant high methane selectivity characteristic of nickel catalysts.[74] In the case of the titania- and niobia-supported samples, a reverse trend was observed, that is, higher TOFs coincide with higher wavenumbers of adsorbed CO. We propose that CO here is weakly bonded to the metal surface, allowing a closer to optimal surface hydrogen coverage.[4,28,75] In contrast to the α-alumina catalysts, CO dissociation is no longer the rate-determining step for reducible supports but more likely the hydrogenation of surface carbon. Similar to MnO on cobalt,[76−79] NbO_x and TiO_x suboxides on the Co−Ni surface might generate active sites with altered effects on the FT mechanism and more specifically accelerate CO dissociation. Following the model of Filot et al.,[4] Co−Ni on reducible supports then diverges from the regime controlled by CO dissociation toward a regime closer to an optimal balance between CO dissociation, carbon hydrogenation, and oxygen removal, similar to Ru.

Additionally, the stability of the catalysts was influenced by the support. Figure S12 shows the relative change in activity during reaction for the different metal compositions supported on niobia, titania, and α-alumina (A, B, and C, respectively). Catalysts containing cobalt and nickel supported on niobia or titania showed similar activity loss as the samples containing only cobalt (~20−25%); however, the largest activity loss was

https://dx.doi.org/10.1021/acscatal.0c00777
ACS Catal. 2020, 10, 7343−7354

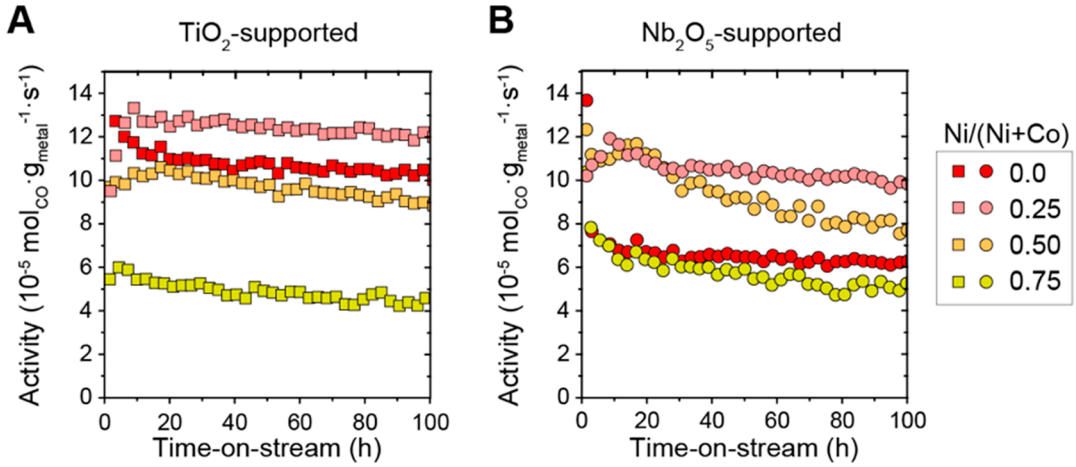

Figure 7. Metal weight-normalized catalytic activity against time on stream for cobalt and cobalt−nickel catalysts supported on reducible metal oxides, (A) on titania and (B) on niobia. Prior to exposure to reaction conditions, samples were reduced in situ at 350 °C in 25 vol % H_2 in He at 1 bar. Reaction conditions: 220 °C, 20 bar and H_2/CO = 2 v/v.

observed for catalysts containing only nickel, 35% for Nb_2O_5 and 55% for TiO_2. For the α-Al_2O_3-supported catalysts, the activity loss increased with increasing nickel content relative to cobalt, with the monometallic cobalt sample being the most stable (25% activity loss) and the monometallic nickel one the least (60% activity loss). Activity loss in nickel-based catalysts under these conditions is often driven by a decrease of nickel specific surface area due to formation and diffusion of volatile nickel tetracarbonyl from small to large nanoparticles and leading to overall particle growth.[80,81] Nickel carbonyl formation can be avoided by alloying nickel with another metal or by the SMSI effect with a reducible oxide as support.[44,45,82,83] This rationalizes the stability of the Co−Ni samples supported on niobia and titania. However, for the monometallic nickel samples supported on reducible oxides, a reduction temperature of 350 °C prior to reaction most likely is not high enough to induce a SMSI state capable of completely hampering nickel tetracarbonyl formation[45] and thus the activity loss.

STEM-EDX of the used niobia-supported Co−Ni catalysts revealed minor changes on the particle size and metal distribution compared to the freshly reduced samples (Figure S2D−F). In the case of the alumina-based catalyst, STEM-EDX of the sample with composition Ni/(Ni + Co) = 0.50 atom/atom (Figure S6D) showed substantial particle growth, 9 nm for the freshly reduced sample against 32 nm for the sample after FT, and areas with nonuniform cobalt and nickel distribution. The extensive particle growth most likely originated from nickel carbonyl formation and diffusion, leading subsequently to a decrease in the catalytic activity. Metal quantification by EDX and ICP analyses showed that the amount of nickel before and after reaction conditions had not changed (Table S4). This suggests that despite the possible formation of $Ni(CO)_4$, the conditions (pressure, time, etc.) were not severe enough to remove a measurable quantity of nickel from the catalyst bed at atmospheric pressure, in agreement with previous research.[81]

Overall, the catalytic performance results at 1 bar show that the combination of reducible oxides as support material together with bimetallic cobalt−nickel nanoparticles have potential as highly active, selective, and stable Fischer−Tropsch catalysts. Therefore, we focused on these samples and the monometallic cobalt ones (Ni/(Ni + Co) = 0.0, 0.25, 0.50, and 0.75 atom/atom) to evaluate their catalytic performance at higher pressures. Due to the likely formation of volatile nickel tetracarbonyl already at 1 bar for samples containing only nickel (Ni/(Ni + Co) = 1.0 atom/atom) and α-Al_2O_3-supported samples containing nickel, experiments at higher pressures were not carried out for these samples to avoid the risk of nickel loss from the catalysts.

The high-pressure Fischer−Tropsch catalytic performance was studied at 220 °C and 20 bar (H_2/CO = 2 v/v) for 100 h on stream. The catalytic activity through time is shown in Figure 7 for the titania- and niobia-supported catalysts (A and B, respectively). Increase in the reaction pressure to 20 bar largely improved the activity of the monometallic and cobalt-rich samples. Particularly samples containing 25% nickel (Ni/(Ni + Co) = 0.25 atom/atom) had an activation period during the first hours of the experiment resulting eventually in the highest metal-normalized activities and turnover frequencies of the set of samples. Comprehensive data after 100 h on stream can be found in Table S2. Similar activation of bimetallic Co−Ni catalysts for FT has been previously observed and attributed to partial segregation of the metals during reaction.[24] Replacement of 50% cobalt by nickel (Ni/(Ni + Co) = 0.50 atom/atom) showed similar activities as the cobalt-based catalysts. However, the nickel-rich samples (Ni/(Ni + Co) = 0.75 atom/atom) did not show an increase in activity by increasing the reaction pressure and thus became the less active catalysts under these conditions.

Selectivity trends were similar for both support materials; the main changes were observed throughout the reaction depending on the Co−Ni composition (Figure S13). Cobalt-rich catalysts showed increased C_{5+} selectivities upon pressure increase. Ni/(Ni + Co) = 0.0 and 0.25 atom/atom samples presented the highest C_{5+} selectivities with 83% for TiO_2 and 86% for Nb_2O_5 (Figure S13A,D, respectively). C_2−C_4 selectivity increased with increasing nickel content (Figure S13B,E). During the first 20 h on stream, a sharp decrease in C_2−C_4 selectivity was observed for all nickel-containing catalysts. At the same time, these samples also showed an initial increase in C_{5+} selectivity during the first 10 h on stream. C_1 selectivities were relatively low for all samples, but no clear trend with nickel content was found (Figure S13C,F). All samples showed an increase in C_1 selectivity at the beginning of the experiment; however, for the bimetallic samples, this

https://dx.doi.org/10.1021/acscatal.0c00777
ACS Catal. 2020, 10, 7343−7354

increase took around 40 h on stream to reach stable values, whereas for the monometallic samples, it occurred during the first 10 h on stream.

In comparison to cobalt−nickel supported on nonreducible oxides from literature, the activity of the niobia- and titania-supported catalysts proved superior at similar reaction conditions, while maintaining similar C_{5+} selectivities (Table S5 and Figure S14). Hence, the promotional effect of reducible oxides on Co−Ni nanoparticles was maintained at high pressures.

STEM-EDX of the used Co−Ni catalysts supported on niobia showed a quite uniform composition in the metal nanoparticles, some particle growth, and some areas of the support depleted of nanoparticles (Figure S2G−I). For the Co-rich sample, nanoparticles containing only cobalt, which were observed after reduction and after low-pressure catalysis (Figure S3), were no longer observed; all nanoparticles contained both cobalt and nickel. Similar changes were observed in the titania-supported Ni/(Ni + Co) = 0.50 atom/atom catalyst (Figure S7). Furthermore, some nanoparticles in the sample with highest initial nickel content (Ni/(Ni + Co) = 0.75 atom/atom) supported on niobia showed a surface enriched with cobalt, confirmed by a cross section of the Co−Ni distribution (Figure S15). The rearrangement of the metals might originate from a structure change during the high-pressure conditions,[84,85] a faster oxidation of cobalt when exposed to air after the experiment accompanied by the Kirkerdall effect,[72,86,87] or nickel interparticle transport related to the high CO partial pressure.[88,89] Quantification of the EDX maps for various samples revealed even a loss in nickel relative to the cobalt content confirmed by ICP (Table S4). Despite the loss of nickel, Co−Ni catalysts compared to the monometallic cobalt showed similar C_{5+} selectivities and higher Fischer−Tropsch activities for the samples Ni/(Ni + Co) = 0.25 atom/atom supported on titania and Ni/(Ni + Co) = 0.25 and 0.50 atom/atom supported on niobia.

The set of samples was additionally studied at higher temperatures, namely, 240 and 260 °C, and 20 bar, since reducible supports have shown potential for operating at high temperatures without sacrificing C_{5+} selectivity.[90] Figures S16 and S17 show a summary of the catalytic performance after 100 h on stream, 20 bar, and 220−260 °C (the exact values can be found in Table S2). A temperature increase magnified the activity trends already observed at 220 °C, in the order 0.25 > 0.50 > 0.0 > 0.75 atom/atom for the niobia-supported samples and 0.25 > 0.0 > 0.50 > 0.75 atom/atom for the titania-supported samples. More surprisingly, selectivity trends drastically changed with the increase in reaction temperature. For both titania- and niobia-supported samples, the increase in temperature resulted in a notorious increase in C_1 and C_2−C_4 products at the expense of C_{5+} ones (Figures S16 and S17, panels B, C, and D). This behavior attenuated upon increasing the nickel content, thus the monometallic cobalt catalysts showed the largest increase in C_1 and C_2−C_4 selectivities, whereas the nickel-rich catalyst (Ni/(Ni + Co) = 0.75 atom/atom) had almost unchanged selectivity upon increasing the reaction temperature. The selectivity trends observed at 220 °C had practically inverted at 260 °C.

Apparent activation energies were derived from the catalytic activities at temperatures of 220−260 °C and plotted as a function of Ni/(Ni + Co) for both supports (Figure 8). At high nickel content (Ni/(Ni + Co) = 0.75 atom/atom), the activation energy increased compared to the monometallic

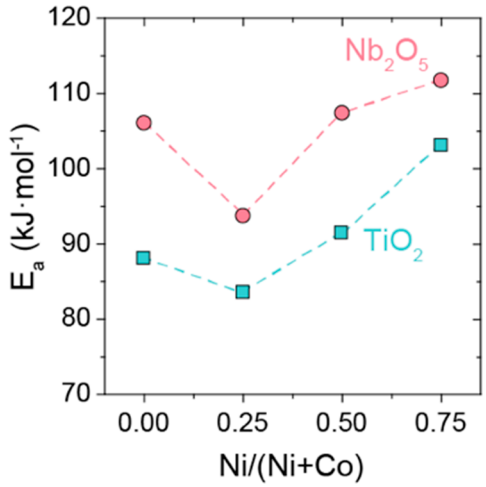

Figure 8. Apparent activation energies for catalysts with different cobalt to nickel ratios supported on titania (blue squares) and niobia (red circles). Apparent activation energies were obtained from the slopes of the Arrhenius equation in the linear form (Figure S18). Reaction conditions: 20 bar, H_2/CO = 2 v/v, after 100 h on stream and temperatures of 220, 240, and 260 °C.

cobalt catalysts on both supports. A substitution of 50% of the cobalt by nickel displayed similar activation energy as for the cobalt-only catalysts. Finally, substitution of cobalt by 25% nickel decreased the activation energy, indicating that up to a certain nickel concentration, it functioned as a promoter, which was also reflected by increased turnover frequencies.

4. CONCLUSION

Bimetallic Co−Ni nanoparticles supported on reducible (TiO_2 and Nb_2O_5) and nonreducible (α-Al_2O_3) oxides were synthesized and characterized, and their catalytic performance in the Fischer−Tropsch (FT) synthesis was evaluated. Samples were prepared by coimpregnation of aqueous solutions with varying cobalt to nickel atomic ratio. After calcination, samples were characterized by TPR where a shift toward lower temperatures in the reduction profiles of the bimetallic samples was observed, in comparison to the monometallic samples, indicative of a close interaction between the cobalt and nickel oxides. TEM of the reduced samples revealed that gradual substitution of cobalt by nickel led to a decrease in nanoparticle size on all support materials. However, comparison of the theoretical and experimental H_2 uptakes (derived from TEM and H_2 chemisorption, respectively) showed a discrepancy for the samples supported on reducible oxides, which was ascribed to the SMSI effect, whereas the samples supported on the nonreducible support did not show this difference. STEM-EDX analysis of the reduced and passivated catalysts demonstrated that while nickel was always found together with cobalt, cobalt could be found without nickel. Nanoparticles containing both metals showed a uniform Co−Ni distribution. Moreover, CO-FTIR results suggested that for the reducible supports, the metal nanoparticles likely underwent a cobalt-enrichment at their surface upon increasing the CO pressure, while the nanoparticles supported on alumina did not. This indicated that the surface composition of the nanoparticles was affected by the metal−support interaction.

The low-pressure catalytic performance showed substantially higher activities, C_{5+} selectivities, and stabilities for the bimetallic nanoparticles supported on reducible oxides. In

https://dx.doi.org/10.1021/acscatal.0c00777
ACS Catal. 2020, 10, 7343−7354

contrast, the alumina-based catalysts showed low activities and C_{5+} selectivities independently of the Co−Ni composition and, moreover, a continuous loss of activity. The marked difference in catalytic performance was tentatively attributed to a shift of the rate-determining step, as derived from the trend between TOF and CO-FTIR. For Co−Ni supported on reducible oxides, a weaker adsorption of CO was inferred, which improves H adsorption and the catalytic activity. The catalytic performances of the samples supported on reducible supports were also studied at 20 bar and various temperatures. At 220 °C, the cobalt-rich samples benefited from the increase in pressure resulting in high activity and C_{5+} selectivities. However, higher reaction temperatures inverted the selectivity trend. Yet, a comparison to nonreducible-supported catalysts from the literature showed the promotional effect of reducible oxides on bimetallic nanoparticles. Twenty-five percent substitution of cobalt by nickel led to lower apparent activation energy values, implying that nickel acted as promotor in these samples. In summary, we showed that the combination of cobalt and nickel supported on reducible oxides allowed for increased FT performance. Reducible oxides used as support material strongly modify the reactivity of bimetallic nanoparticles thus opening up avenues to arrive at more efficient catalysts.

■ ASSOCIATED CONTENT

Supporting Information

The Supporting Information is available free of charge at https://pubs.acs.org/doi/10.1021/acscatal.0c00777.

Additional characterization and catalytic results, complete catalytic data, and literature comparison (PDF)

■ AUTHOR INFORMATION

Corresponding Author

Krijn P. de Jong − *Inorganic Chemistry and Catalysis, Debye Institute for Nanomaterials Science, Utrecht University, 3584 CG Utrecht, The Netherlands;* orcid.org/0000-0002-9773-8110; Email: k.p.dejong@uu.nl

Authors

Carlos Hernández Mejía − *Inorganic Chemistry and Catalysis, Debye Institute for Nanomaterials Science, Utrecht University, 3584 CG Utrecht, The Netherlands;* orcid.org/0000-0002-1313-2956

Jessi E. S. van der Hoeven − *Inorganic Chemistry and Catalysis, Debye Institute for Nanomaterials Science and Soft Condensed Matter, Debye Institute for Nanomaterials Science, Utrecht University, 3584 CG Utrecht, The Netherlands;* orcid.org/0000-0001-9832-289X

Petra E. de Jongh − *Inorganic Chemistry and Catalysis, Debye Institute for Nanomaterials Science, Utrecht University, 3584 CG Utrecht, The Netherlands;* orcid.org/0000-0002-2216-2620

Complete contact information is available at: https://pubs.acs.org/10.1021/acscatal.0c00777

Notes

The authors declare no competing financial interest.

■ ACKNOWLEDGMENTS

Companhia Brasileira de Metalurgia e Mineração (CBMM) is thanked for financial support. K.P.d.J. acknowledges support from the European Research Council, EU FP7 ERC Advanced Grant No. 338846. J.E.S.v.d.H. and P.d.J. acknowledge funding from the European Research Council (ERC) under the European Union's Horizon 2020 research and innovation programme (ERC-2014-CoG No 648991). Savannah Turner (Utrecht University) is acknowledged for performing TEM measurements. Miguel Rivera-Torrente, Zanoni Silvia, and Herrick Schaink (Utrecht University) are thanked for their assistance and support during the CO-FTIR measurements. Lennart Weber and Tom W. van Deelen (Utrecht University) are thanked for their support during the catalytic performance and fruitful discussions throughout the project.

■ REFERENCES

(1) Chu, S.; Majumdar, A. Opportunities and Challenges for a Sustainable Energy Future. *Nature* **2012**, *488*, 294−303.

(2) Staples, M. D.; Malina, R.; Barrett, S. R. H. The Limits of Bioenergy for Mitigating Global Life-Cycle Greenhouse Gas Emissions from Fossil Fuels. *Nat. Energy* **2017**, *2*, 16202.

(3) Armstrong, R. C.; Wolfram, C.; de Jong, K. P.; Gross, R.; Lewis, N. S.; Boardman, B.; Ragauskas, A. J.; Ehrhardt-Martinez, K.; Crabtree, G.; Ramana, M. V. The Frontiers of Energy. *Nat. Energy* **2016**, *1*, 15020.

(4) Filot, I. A. W.; Van Santen, R. A.; Hensen, E. J. M. The Optimally Performing Fischer−Tropsch Catalyst. *Angew. Chem., Int. Ed.* **2014**, *53*, 12746−12750.

(5) Chen, W.; Filot, I. A. W.; Pestman, R.; Hensen, E. J. M. Mechanism of Cobalt-Catalyzed CO Hydrogenation: 2. *ACS Catal.* **2017**, *7*, 8061−8071.

(6) Van Santen, R. A.; Markvoort, A. J.; Ghouri, M. M.; Hilbers, P. A. J.; Hensen, E. J. M. Monomer Formation Model versus Chain Growth Model of the Fischer−Tropsch Reaction. *J. Phys. Chem. C* **2013**, *117*, 4488−4504.

(7) Besenbacher, F.; Chorkendorff, I.; Clausen, B. S.; Hammer, B.; Molenbroek, A. M.; Nørskov, J. K.; Stensgaard, I. Design of a Surface Alloy Catalyst for Steam Reforming. *Science* **1998**, *279*, 1913−1915.

(8) Ferrando, R.; Jellinek, J.; Johnston, R. L. Nanoalloys: From Theory to Applications of Alloy Clusters and Nanoparticles. *Chem. Rev.* **2008**, *108*, 845−910.

(9) Calderone, V. R.; Shiju, N. R.; Ferré, D. C.; Rothenberg, G. Bimetallic Catalysts for the Fischer−Tropsch Reaction. *Green Chem.* **2011**, *13*, 1950−1959.

(10) Jacobsen, C. J. H.; Dahl, S.; Clausen, B. G. S.; Bahn, S.; Logadottir, A.; Nørskov, J. K. Catalyst Design by Interpolation in the Periodic Table: Bimetallic Ammonia Synthesis Catalysts. *J. Am. Chem. Soc.* **2001**, *123*, 8404−8405.

(11) Dry, M. E. The Fischer−Tropsch Process: 1950−2000. *Catal. Today* **2002**, *71*, 227−241.

(12) Cheng, K.; Kang, J.; King, D. L.; Subramanian, V.; Zhou, C.; Zhang, Q.; Wang, Y. Advances in Catalysis for Syngas Conversion to Hydrocarbons. *Adv. Catal.* **2017**, *60*, 125−208.

(13) Pan, W. X.; Cao, R.; Griffin, G. L. Direct Alcohol Synthesis Using Copper/Cobalt Catalysts. *J. Catal.* **1988**, *114*, 447−456.

(14) Prieto, G.; Beijer, S.; Smith, M. L.; He, M.; Au, Y.; Wang, Z.; Bruce, D. A.; De Jong, K. P.; Spivey, J. J.; De Jongh, P. E. Design and Synthesis of Copper-Cobalt Catalysts for the Selective Conversion of Synthesis Gas to Ethanol and Higher Alcohols. *Angew. Chem., Int. Ed.* **2014**, *53*, 6397−6401.

(15) Xiang, Y.; Barbosa, R.; Li, X.; Kruse, N. Ternary Cobalt-Copper-Niobium Catalysts for the Selective CO Hydrogenation to Higher Alcohols. *ACS Catal.* **2015**, *5*, 2929−2934.

(16) Calderone, V. R.; Shiju, N. R.; Curulla-Ferré, D.; Chambrey, S.; Khodakov, A.; Rose, A.; Thiessen, J.; Jess, A.; Rothenberg, G. De Novo Design of Nanostructured Iron-Cobalt Fischer−Tropsch Catalysts. *Angew. Chem., Int. Ed.* **2013**, *52*, 4397−4401.

(17) Griboval-Constant, A.; Butel, A.; Ordomsky, V. V.; Chernavskii, P. A.; Khodakov, A. Y. Cobalt and Iron Species in Alumina Supported

Bimetallic Catalysts for Fischer−Tropsch Reaction. *Appl. Catal., A* **2014**, *481*, 116−126.
(18) Enger, B. C.; Holmen, A. Nickel and Fischer−Tropsch Synthesis. *Catal. Rev.: Sci. Eng.* **2012**, *54*, 437−488.
(19) Ishihara, T.; Horiuchi, N.; Inoue, T.; Eguchi, K.; Takita, Y.; Arai, H. Effect of Alloying on CO Hydrogenation Activity over SiO2-Supported CoNi Alloy Catalysts. *J. Catal.* **1992**, *136*, 232−241.
(20) Shimura, K.; Miyazawa, T.; Hanaoka, T.; Hirata, S. Fischer−Tropsch Synthesis over Alumina Supported Bimetallic Co-Ni Catalyst: Effect of Impregnation Sequence and Solution. *J. Mol. Catal. A: Chem.* **2015**, *407*, 15−24.
(21) Das, P. C.; Pradhan, N. C.; Dalai, A. K.; Bakshi, N. N. Carbon Monoxide Hydrogenation over Zirconia Supported Ni and Co-Ni Bimetallic Catalysts. *Catal. Lett.* **2004**, *98*, 153−160.
(22) Razzaq, R.; Zhu, H.; Jiang, L.; Muhammad, U.; Li, C.; Zhang, S. Catalytic Methanation of CO and CO2 in Coke Oven Gas over Ni-Co/ZrO2-CeO2. *Ind. Eng. Chem. Res.* **2013**, *52*, 2247−2256.
(23) van Helden, P.; Prinsloo, F.; van den Berg, J. A.; Xaba, B.; Erasmus, W.; Claeys, M.; van de Loosdrecht, J. Cobalt-Nickel Bimetallic Fischer−Tropsch Catalysts: A Combined Theoretical and Experimental Approach. *Catal. Today* **2020**, *342*, 88−98.
(24) Rytter, E.; Skagseth, T. H.; Eri, S.; Sjåstad, A. O. Cobalt Fischer−Tropsch Catalysts Using Nickel Promoter as a Rhenium Substitute to Suppress Deactivation. *Ind. Eng. Chem. Res.* **2010**, *49*, 4140−4148.
(25) Arai, H.; Mitsuishi, K.; Seiyama, T. TiO2-Supported Fe−Co, Co−Ni, and Ni−Fe Alloy Catalysts for Fischer−Tropsch Synthesis. *Chem. Lett.* **1984**, *13*, 1291−1294.
(26) Ishihara, T.; Eguchi, K.; Arai, H. Hydrogenation of Carbon Monoxide over SiO2-Supported Fe-Co, Co-Ni and Ni-Fe Bimetallic Catalysts. *Appl. Catal.* **1987**, *30*, 225−238.
(27) Ishihara, T.; Horiuchi, N.; Eguchi, K.; Arai, H. The Effect of Supports on the Activity and Selectivity of CoNi Alloy Catalysts for CO Hydrogenation. *J. Catal.* **1991**, *130*, 202−211.
(28) Ishihara, T.; Eguchi, K.; Arai, H. Importance of Surface Hydrogen Concentration in Enhancing Activity of CoNi Alloy Catalyst for CO Hydrogenation. *J. Mol. Catal.* **1992**, *72*, 253−261.
(29) van Deelen, T. W.; Hernández Mejía, C.; de Jong, K. P. Control of Metal-Support Interactions in Heterogeneous Catalysts to Enhance Activity and Selectivity. *Nat. Catal.* **2019**, *2*, 955−970.
(30) Cuenya, B. R. Synthesis and Catalytic Properties of Metal Nanoparticles: Size, Shape, Support, Composition, and Oxidation State Effects. *Thin Solid Films* **2010**, *518*, 3127−3150.
(31) Divins, N. J.; Angurell, I.; Escudero, C.; Pérez-Dieste, V.; Llorca, J. Influence of the Support on Surface Rearrangements of Bimetallic Nanoparticles in Real Catalysts. *Science* **2014**, *346*, 620−623.
(32) Han, C. W.; Majumdar, P.; Marinero, E. E.; Aguilar-Tapia, A.; Zanella, R.; Greeley, J.; Ortalan, V. Highly Stable Bimetallic AuIr/TiO2 Catalyst: Physical Origins of the Intrinsic High Stability against Sintering. *Nano Lett.* **2015**, *15*, 8141−8147.
(33) Destro, P.; Kokumai, T. M.; Scarpellini, A.; Pasquale, L.; Manna, L.; Colombo, M.; Zanchet, D. The Crucial Role of the Support in the Transformations of Bimetallic Nanoparticles and Catalytic Performance. *ACS Catal.* **2018**, *8*, 1031−1037.
(34) Gubó, R.; Yim, C. M.; Allan, M.; Pang, C. L.; Berkó, A.; Thornton, G. Variation of SMSI with the Au:Pd Ratio of Bimetallic Nanoparticles on TiO2(110). *Top. Catal.* **2018**, *61*, 308−317.
(35) Mouaddib, N.; Perrichon, V.; Primet, M. Bulk and Surface Characterization of Supported Cobalt-Copper Catalysts Active in CO Hydrocondensation. *J. Chem. Soc., Faraday Trans. 1* **1989**, *85*, 3413−3424.
(36) Tauster, S. J.; Fung, S. C.; Garten, R. L. Strong Metal-Support Interactions. Group 8 Noble Metals Supported on Titanium Dioxide. *J. Am. Chem. Soc.* **1978**, *100*, 170−175.
(37) Tauster, S. J. Strong Metal-Support Interactions. *Acc. Chem. Res.* **1987**, *20*, 389−394.
(38) Reuel, R. C.; Bartholomew, C. H. Effects of Support and Dispersion on the CO Hydrogenation Activity/Selectivity Properties of Cobalt. *J. Catal.* **1984**, *85*, 78−88.
(39) Johnson, G. R.; Bell, A. T. Effects of Lewis Acidity of Metal Oxide Promoters on the Activity and Selectivity of Co-Based Fischer−Tropsch Synthesis Catalysts. *J. Catal.* **2016**, *338*, 250−264.
(40) Prieto, G.; De Mello, M. I. S.; Concepción, P.; Murciano, R.; Pergher, S. B. C.; Martínez, A. Cobalt-Catalyzed Fischer−Tropsch Synthesis: Chemical Nature of the Oxide Support as a Performance Descriptor. *ACS Catal.* **2015**, *5*, 3323−3335.
(41) Boffa, A. B.; Lin, C.; Bell, A. T.; Somorjai, G. A. Lewis Acidity as an Explanation for Oxide Promotion of Metals: Implications of Its Importance and Limits for Catalytic Reactions. *Catal. Lett.* **1994**, *27*, 243−249.
(42) Maitlis, P. M.; Zanotti, V. The Role of Electrophilic Species in the Fischer−Tropsch Reaction. *Chem. Commun.* **2009**, *13*, 1619−1634.
(43) Hernández Mejía, C.; van Deelen, T. W.; de Jong, K. P. Activity Enhancement of Cobalt Catalysts by Tuning Metal-Support Interactions. *Nat. Commun.* **2018**, *9*, 4459.
(44) Vannice, M. A.; Garten, R. L. Metal-Support Effects on the Activity and Selectivity of Ni Catalysts in CO/H_2 Synthesis Reactions. *J. Catal.* **1979**, *56*, 236−248.
(45) Hernández Mejía, C.; Vogt, C.; Weckhuysen, B. M.; De Jong, K. P. Stable Niobia-Supported Nickel Catalysts for the Hydrogenation of Carbon Monoxide to Hydrocarbons. *Catal. Today* **2020**, *343*, 56−62.
(46) Schindelin, J.; Arganda-Carreras, I.; Frise, E.; Kaynig, V.; Longair, M.; Pietzsch, T.; Preibisch, S.; Rueden, C.; Saalfeld, S.; Schmid, B.; Tinevez, J. Y.; White, D. J.; Hartenstein, V.; Eliceiri, K.; Tomancak, P.; Cardona, A. Fiji: An Open-Source Platform for Biological-Image Analysis. *Nat. Methods* **2012**, *9*, 676−682.
(47) Voss, G. J. B.; Fløystad, J. B.; Voronov, A.; Rønning, M. The State of Nickel as Promotor in Cobalt Fischer−Tropsch Synthesis Catalysts. *Top. Catal.* **2015**, *58*, 896−904.
(48) Tauster, S. J.; Fung, S. C. Strong Metal-Support Interactions: Occurrence among the Binary Oxides of Groups IIA-VB. *J. Catal.* **1978**, *55*, 29−35.
(49) Lögdberg, S.; Yang, J.; Lualdi, M.; Walmsley, J. C.; Järås, S.; Boutonnet, M.; Blekkan, E. A.; Rytter, E.; Holmen, A. Further Insights into Methane and Higher Hydrocarbons Formation over Cobalt-Based Catalysts with Γ-Al2O3, A-Al2O3 and TiO2 as Support Materials. *J. Catal.* **2017**, *352*, 515−531.
(50) Van Der Hoeven, J. E. S.; Welling, T. A. J.; Silva, T. A. G.; Van Den Reijen, J. E.; La Fontaine, C.; Carrier, X.; Louis, C.; Van Blaaderen, A.; De Jongh, P. E. In Situ Observation of Atomic Redistribution in Alloying Gold-Silver Nanorods. *ACS Nano* **2018**, *12*, 8467−8476.
(51) Ansorge, J.; Förster, H. Transient Ir Spectroscopic Investigation of Surface-Carbonyl Formation on a Supported Cobalt Catalyst. *J. Catal.* **1981**, *68*, 182−185.
(52) Lapidus, A.; Krylova, A.; Kazanskii, V.; Borovkov, V.; Zaitsev, A.; Rathousky, J.; Zukal, A.; Jančálková, M. Hydrocarbon Synthesis from Carbon Monoxide and Hydrogen on Impregnated Cobalt Catalysts Part I. Physico-Chemical Properties of 10% Cobalt/Alumina and 10% Cobalt/Silica. *Appl. Catal.* **1991**, *73*, 65−81.
(53) Beitel, G. A.; Laskov, A.; Oosterbeek, H.; Kuipers, E. W. Polarization Modulation Infrared Reflection Absorption Spectroscopy of CO Adsorption on Co(0001) under a High-Pressure Regime. *J. Phys. Chem.* **1996**, *100*, 12494−12502.
(54) Sun, S.; Tsubaki, N.; Fujimoto, K. The Reaction Performances and Characterization of Fischer−Tropsch Synthesis Co/SiO2 Catalysts Prepared from Mixed Cobalt Salts. *Appl. Catal., A* **2000**, *202*, 121−131.
(55) Prieto, G.; Martínez, A.; Concepción, P.; Moreno-Tost, R. Cobalt Particle Size Effects in Fischer−Tropsch Synthesis: Structural and in Situ Spectroscopic Characterisation on Reverse Micelle-Synthesised Co/ITQ-2 Model Catalysts. *J. Catal.* **2009**, *266*, 129−144.

https://dx.doi.org/10.1021/acscatal.0c00777
ACS Catal. 2020, 10, 7343−7354

(56) Kadinov, G.; Bonev, C.; Todorova, S.; Palazov, A. IR Spectroscopy Study of CO Adsorption and of the Interaction between CO and Hydrogen on Alumina-Supported Cobalt. *J. Chem. Soc., Faraday Trans.* **1998**, *94*, 3027−3031.
(57) Dalmon, J. A.; Primet, M.; Martin, G. A.; Imelik, B. Magnetic and Infrared Study of CO Chemisorption on Silica Supported Nickel-Copper Alloys. *Surf. Sci.* **1975**, *50*, 95−108.
(58) Trenary, M.; Uram, K. J.; Yates, J. T. An Infrared Reflection-Absorption Study of CO Chemisorbed on Clean and Sulfided Ni(111) - Evidence for Local Surface Interactions. *Surf. Sci.* **1985**, *157*, 512−538.
(59) Agnelli, M.; Swaan, H. M.; Marquez-Alvarez, C.; Martin, G. A.; Mirodatos, C. CO Hydrogenation on a Nickel Catalyst: II. A Mechanistic Study by Transient Kinetics and Infrared Spectroscopy. *J. Catal.* **1998**, *175*, 117−128.
(60) Van Santen, R. A. Coordination of Carbon Monoxide to Transition-Metal Surfaces. *J. Chem. Soc., Faraday Trans. 1* **1987**, *83*, 1915−1934.
(61) Mihaylov, M.; Hadjiivanov, K.; Knözinger, H. Formation of Ni(CO)4 during the Interaction between CO and Silica-Supported Nickel Catalyst: An FTIR Spectroscopic Study. *Catal. Lett.* **2001**, *76*, 59−63.
(62) Jensen, M. B.; Morandi, S.; Prinetto, F.; Sjåstad, A. O.; Olsbye, U.; Ghiotti, G. FT-IR Characterization of Supported Ni-Catalysts: Influence of Different Supports on the Metal Phase Properties. *Catal. Today* **2012**, *197*, 38−49.
(63) Primet, M. Electronic Transfer and Ligand Effects in the Infrared Spectra of Adsorbed Carbon Monoxide. *J. Catal.* **1984**, *88*, 273−282.
(64) Toyoshima, I.; Somorjai, G. A. Heats of Chemisorption of O2, H2, CO, CO2, and N2 on Polycrystalline and Single Crystal Transition Metal Surfaces. *Catal. Rev.: Sci. Eng.* **1979**, *19*, 105−159.
(65) Bridge, M. E.; Comrie, C. M.; Lambert, R. M. Chemisorption Studies on Cobalt Single Crystal Surfaces. *Surf. Sci.* **1977**, *67*, 393−404.
(66) Brennan, D.; Hayes, F. H. The Adsorption of Carbon Monoxide on Evaporated Metal Films. *Philos. Trans. R. Soc. A Math. Phys. Eng. Sci.* **1965**, *258*, 375−386.
(67) Bonzel, H. P.; Krebs, H. J. Surface Science Approach to Heterogeneous Catalysis: CO Hydrogenation on Transition Metals. *Surf. Sci.* **1982**, *117*, 639−658.
(68) Abild-Pedersen, F.; Andersson, M. P. CO Adsorption Energies on Metals with Correction for High Coordination Adsorption Sites - A Density Functional Study. *Surf. Sci.* **2007**, *601*, 1747−1753.
(69) Miyazaki, E. Chemisorption of Diatomic Molecules (H2, N2, CO) on Transition d-Metals. *J. Catal.* **1980**, *65*, 84−94.
(70) Blyholder, G. Molecular Orbital View of Chemisorbed Carbon Monoxide. *J. Phys. Chem.* **1964**, *68*, 2772−2777.
(71) Bailliard-Letournel, R. M.; Gomez Cobo, A. J.; Mirodatos, C.; Primet, M.; Dalmon, J. A. About the Nature of the Co-Cu Interaction in Co-Based Catalysts for Higher Alcohols Synthesis. *Catal. Lett.* **1989**, *2*, 149−156.
(72) Law, Y. T.; Dintzer, T.; Zafeiratos, S. Surface Oxidation of NiCo Alloy: A Comparative X-Ray Photoelectron Spectroscopy Study in a Wide Pressure Range. *Appl. Surf. Sci.* **2011**, *258*, 1480−1487.
(73) Braunschweig, E. J.; Logan, A. D.; Datye, A. K.; Smith, D. J. Reversibility of Strong Metal-Support Interactions on RhTiO2. *J. Catal.* **1989**, *118*, 227−237.
(74) Sehested, J.; Dahl, S.; Jacobsen, J.; Rostrup-Nielsen, J. R. Methanation of CO over Nickel: Mechanism and Kinetics at High H 2/CO Ratios. *J. Phys. Chem. B* **2005**, *109*, 2432−2438.
(75) Weststrate, C. J.; Niemantsverdriet, J. W. Understanding FTS Selectivity: The Crucial Role of Surface Hydrogen. *Faraday Discuss.* **2017**, *197*, 101−116.
(76) Dinse, A.; Aigner, M.; Ulbrich, M.; Johnson, G. R.; Bell, A. T. Effects of Mn Promotion on the Activity and Selectivity of Co/SiO 2 for Fischer−Tropsch Synthesis. *J. Catal.* **2012**, *288*, 104−114.
(77) Johnson, G. R.; Werner, S.; Bell, A. T. An Investigation into the Effects of Mn Promotion on the Activity and Selectivity of Co/SiO2 for Fischer−Tropsch Synthesis: Evidence for Enhanced CO Adsorption and Dissociation. *ACS Catal.* **2015**, *5*, 5888−5903.
(78) Pedersen, E. Ø.; Svenum, I. H.; Blekkan, E. A. Mn Promoted Co Catalysts for Fischer−Tropsch Production of Light Olefins − An Experimental and Theoretical Study. *J. Catal.* **2018**, *361*, 23−32.
(79) Athariboroujeny, M.; Raub, A.; Iablokov, V.; Chenakin, S.; Kovarik, L.; Kruse, N. Competing Mechanisms in CO Hydrogenation over Co-MnOx Catalysts. *ACS Catal.* **2019**, *9*, 5603−5612.
(80) Mirodatos, C.; Praliaud, H.; Primet, M. Deactivation of Nickel-Based Catalysts during CO Methanation and Disproportionation. *J. Catal.* **1987**, *107*, 275−287.
(81) Munnik, P.; Velthoen, M. E. Z.; De Jongh, P. E.; De Jong, K. P.; Gommes, C. J. Nanoparticle Growth in Supported Nickel Catalysts during Methanation Reaction - Larger Is Better. *Angew. Chem., Int. Ed.* **2014**, *53*, 9493−9497.
(82) Pereira, E. B.; Martin, G. A. Alcohol Synthesis from Syngas over Nickel Catalysts: Effect of Copper and Lithium Addition. *Appl. Catal., A* **1993**, *103*, 291−309.
(83) Agnelli, M.; Mirodatos, C. CO Hydrogenation on Nickel-Based Catalysts: Effects of Copper Addition. *J. Catal.* **2000**, *192*, 204−214.
(84) Zegkinoglou, I.; Pielsticker, L.; Han, Z. K.; Divins, N. J.; Kordus, D.; Chen, Y. T.; Escudero, C.; Pérez-Dieste, V.; Zhu, B.; Gao, Y.; Cuenya, B. R. Surface Segregation in CuNi Nanoparticle Catalysts during CO 2 Hydrogenation: The Role of CO in the Reactant Mixture. *J. Phys. Chem. C* **2019**, *123*, 8421−8428.
(85) Zafeiratos, S.; Piccinin, S.; Teschner, D. Alloys in Catalysis: Phase Separation and Surface Segregation Phenomena in Response to the Reactive Environment. *Catal. Sci. Technol.* **2012**, *2*, 1787−1801.
(86) Carenco, S.; Wu, C. H.; Shavorskiy, A.; Alayoglu, S.; Somorjai, G. A.; Bluhm, H.; Salmeron, M. Synthesis and Structural Evolution of Nickel-Cobalt Nanoparticles under H2 and CO2. *Small* **2015**, *11*, 3045−3053.
(87) Yin, Y.; Rioux, R. M.; Erdonmez, C. K.; Hughes, S.; Somorjal, G. A.; Alivisatos, A. P. Formation of Hollow Nanocrystals Through the Nanoscale Kirkendall Effect. *Science* **2004**, *304*, 711−714.
(88) Shen, W. M.; Dumesic, J. A.; Hill, C. G. Criteria for Stable Ni Particle Size under Methanation Reaction Conditions: Nickel Transport and Particle Size Growth via Nickel Carbonyl. *J. Catal.* **1981**, *68*, 152−165.
(89) Goldberger, W. M.; Othmer, D. F. Kinetics of Nickel Carbonyl Formation. *Ind. Eng. Chem. Process Des. Dev.* **1963**, *2*, 202−209.
(90) Den Otter, J. H.; De Jong, K. P. Highly Selective and Active Niobia-Supported Cobalt Catalysts for Fischer−Tropsch Synthesis. *Top. Catal.* **2014**, *57*, 445−450.

https://dx.doi.org/10.1021/acscatal.0c00777
ACS Catal. 2020, 10, 7343−7354